RESEARCH PAPERS

Acta Cryst. (1997). D53, 8–22

Multiwavelength Anomalous Diffraction of Sulfite Reductase Hemoprotein: Making the Most of MAD Data

BRIAN R. CRANE,[a] HENRY BELLAMY[b] AND ELIZABETH D. GETZOFF[a]*

[a]*Department of Molecular Biology, The Scripps Research Institute, La Jolla, CA 92037, USA, and* [b]*Stanford Synchrotron Radiation Laboratory, Stanford, CA 94309, USA. E-mail: edg@scripps.edu*

(Received 8 February 1996; accepted 31 May 1996)

Abstract

The structure of the 60 kDa *E. coli* sulfite reductase hemoprotein (SiRHP) was determined by using multiwavelength anomalous diffraction (MAD) to exploit the relatively small anomalous signals produced near the Fe *K* absorption edge from the protein's native Fe_4S_4 cluster and siroheme Fe atom. Because of systematic measurement error, generation of useful MAD data required rejection of outlying intensity observations that were only identified by careful manual scrutiny of the observed intensities and single parameter scaling among wedges of diffraction data. The key steps for obtaining effective phases were local anisotropic scaling between Bijvoet pairs and among wavelengths, extraction of phase information from unmerged observations, and refinement of the anomalous scattering model. Important factors for positioning the anomalous scattering model included removal of aberrant coefficients from Patterson syntheses, positional refinement of the Fe positions against MAD-derived normal-scattering amplitudes, and systematic searches of cluster orientation that attempted to optimize agreement between observed and calculated MAD intensities. To obtain MAD phases for reflections that were underdetermined for least-squares methods, parameters necessary for defining phase-probability distributions had to be estimated from the anomalous scattering model. The MAD phase distributions, when combined probabilistically with otherwise insufficient MIR phase information, led to the determination of the SiRHP structure. The techniques developed and lessons learned from the SiRHP MAD experiment should be applicable to the design of MAD experiments on other macromolecules.

1. Introduction

With the increased accessibility of synchrotron beamlines configured for protein crystallography, multiwavelength anomalous diffraction (MAD) is fast becoming a popular and effective means for phase determination of new macromolecular structures (Hendrickson, 1991). In a MAD experiment, heavy-atom inner-shell electronic transitions result in wavelength-dependent intensity perturbations of the scattered X-rays, from which phase information can be extracted. We have used such anomalous scattering effects to determine the crystal structure of *E. coli* sulfite reductase hemoprotein (SiRHP).

Sulfite and nitrite reductases are responsible for the six-electron reductions of sulfite and nitrite in both assimilatory and dissimilatory metabolism (Peck & Lissolo, 1988). These enzymes contain a unique active center consisting of a siroheme (a tetrahydroporphyrin of the isobacteriochlorin class) covalently coupled to an Fe_4S_4 cluster through a bridging thiolate ligand (Crane, Siegel & Getzoff, 1995). The *E. coli* assimilatory sulfite reductase consists of four catalytic 64 kDa hemoprotein subunits and eight electron-supplying 66 kDa flavoprotein subunits (Siegel & Davis, 1974). The catalytic hemoprotein subunits can be dissociated from the holoenzyme and are completely active when supplied with suitable electron donors (Siegel & Davis, 1974). SiRHP crystallizes in space group $P2_12_12_1$ (cell dimensions $69.75 \times 77.44 \times 87.79$ Å) with one 60 kDa subunit containing five Fe atoms in each asymmetric unit (Crane *et al.*, 1995). [The 64 kDa native protein's N-terminal 73 residues have been proteolytically cleaved from the crystallized species (Crane *et al.*, 1995)]. Initial heavy-atom scans provided a single strong ethyl mercurithiosalicylate (EMTS) derivative (McRee, Richardson, Richardson, & Siegel, 1986), but subsequent comprehensive screening of over 180 conditions provided only a few additional weak derivatives (Crane *et al.*, 1995). Unfortunately, the quality of the multiple isomorphous replacement (MIR) maps could not support a chain trace.

MAD allowed us to exploit the *K*-edge anomalous scattering properties of SiRHP's native Fe atoms for phase determination. The anomalous scattering perturbations for first-row transition metal *K*-edge absorptions are not nearly as pronounced as those for the *L* edges of lanthanides and other heavier elements. As well, the relatively low-energy X-ray radiation exciting the *K*-edge transitions (~7.1 keV for Fe) is susceptible to significant

intensity loss because of air, solvent and crystal absorption. Metal clusters pose additional problems for MAD phasing. At higher than ~2.8 Å resolution, scattering from different cluster Fe atoms is no longer correlated, and this results in a reduction in their anomalous signal by approximately the square root of their number. Yet, measurable anomalous differences from higher resolution data are needed to distinguish the individual Fe-atom positions. An accurate model for the anomalous scatterers is critical for effective MAD phase determination because the phases of all reflections depend on these parameters. MAD phasing from the Fe atoms of iron–sulfur clusters is potentially complicated by the additional anomalous scattering of sulfur at iron-edge energies. Two iron–sulfur proteins, ferredoxin (eight Fe atoms per 5.9 kDa monomer) (Murthy, Hendrickson, Orme-Johnson, Merritt & Phizackerley, 1988) and glutamine 5-phosphoribosyl-1-pyrophosphate (PRPP) amidotransferase (four Fe atoms per 50 kDa monomer) (Smith *et al.*, 1994) have been phased by MAD alone to only ~5 Å resolution. For PRPP amidotransferase, solvent flattening with fourfold symmetry averaging was required to extend the resolution sufficiently for a structure determination. Thus, the successful use of MAD phasing for SiRHP can provide useful information about the robustness and generality of applying MAD to large iron–sulfur cluster containing enzymes.

Although the native anomalous signal from SiRHP was small relative to the normal scattering of the unit cell, we could combine any MAD-derived phase restraints with the existing marginal MIR phases. At the time of the experiment in 1992, the Stanford Synchrotron Radiation Laboratory's (SSRL) area detector beamline (I-5AD) was one of the few accessible facilities with the capability of performing a MAD protein experiment at the iron *K*-absorption edge. In 1992, this beamline was limited by low X-ray intensity (approximately comparable to that from a rotating-anode generator) and the saturability of the multiwire detector. Weak incomplete non-redundant diffraction data complicated all stages of the MAD structure determination, often making the prospects for success discouraging. In order to extract a usable anomalous signal, multiple strategies were applied for data reduction, scaling, Fe-atom positional refinement and phasing. It was often necessary to decide between increasing the overall completeness of unique data or discarding questionable measurements. The identification of especially aberrant outliers was critical for improving the quality of the ultimate phase set. Despite these difficulties, this experiment did lead to a 1.6 Å resolution structure of SiRHP (Crane *et al.*, 1995), demonstrating that when conventional MIR approaches fail, effective MAD phasing can be achieved even for large proteins with far from ideal data sets. Moreover, the methods that were used to overcome limitations in the experimental parameters and data quality may prove useful for other systems.

2. Experimental

2.1. *MAD data collection*

MAD data on SiRHP were collected over a three-week period in April 1992 at area detector beamline I-5AD of the SSRL (Phizackerley, Cork & Merritt, 1986). The 3.0 GeV SPEAR storage ring typically delivered an initial ring current of ~80 mA that decayed to ~40 mA over a 12 h period. The double Si(111) monochromator could select energies over a spectral range of 4–24 keV with motor step increments of ~0.2 eV at 7 keV. At the Fe *K* absorption edge (7.1112 keV or 1.7435 Å), the Flux/mA was 3.4×10^{11} photons for a 1×1 mm aperture, with $d\lambda/\lambda = 2 \times 10^{-4}$. Harmonic energies diffracted from the monochromator were excluded by making the monochromator crystals slightly non-parallel with a piezoelectric driver until the beam intensity was attenuated by 10%. The beamline was equipped with a four-circle diffractometer and a single 28×28 cm Xuong–Hamlin multiwire proportional counter (Mark II) (Hamlin, 1985), with a spatial resolution of 2.00 mm over 144 pixels in x (typically along the φ or spindle axis) and 1.15 mm over 256 pixels in y (perpendicular to the plane formed by the beam and spindle axis). The delay time for signal transmission along the x direction was periodically readjusted to assure uniform sensitivity across the detector face. Detector uniformity was monitored by examining the water-ring scattering, which extended across the approximate center of the detector.

Intensity differences caused by anomalous scattering were maximized by collecting data with two energies at the Fe *K* edge and with one energy remote from the edge, where the dispersive correction was small. $E_B = 7135.9$ eV ($\lambda_B = 1.7374$ Å) and $E_C = 7120.4$ eV ($\lambda_C = 1.7412$ Å) were chosen to maximize the anomalous (f'') and dispersive (f') components of the resonance scattering vector, respectively (Table 1). A third wavelength, $E_A = 8041.1$ eV ($\lambda_A = 1.5418$ Å), was chosen to provide a large dispersive difference when compared with E_B or E_C and also to allow direct comparison with data collected previously from a Cu $K\alpha$ source. Hemoprotein edge energies and anomalous-scattering correction components (f' and f'') were determined by X-ray fluorescence spectroscopy for three crystal orientations that each had one of the three principal reciprocal-space axes coincident with the horizontally polarized electric vector of the synchrotron beam (Fig. 1). The edge energy and scattering factors were not markedly anisotropic in the crystal and thus diffraction data were collected at the same energies for all crystal orientations. Data frames were collected successively at each of the three energies during progression through reciprocal space to limit variability introduced by pathlength-dependent absorption differences, instrument-associated error, radiation decay or crystal slippage. The monochromator

was calibrated relative to the K edge of metallic iron foil (7111.2 eV) by absorption scans and was repeatedly checked and reset throughout the experiment (particularly after the synchrotron ring was filled). The drift was never larger than four motor steps (~0.8 eV).

Multiwire detectors have what is effectively a dead time because they use delay lines to assign pairs of spatial coordinates (x, y) to the detected X-ray photon. If two photons are detected within the maximum transit time of the delay lines both are rejected by the detector electronics as being 'coincident'. Compensating for the loss of counts arising from simultaneous events was crucial, as judged by the degradation in data quality when coincidence corrections were inadvertently not applied (see Fig. 2). Such detector coincidence loss was corrected by extending the exposure of each oscillation step according to the fraction of event loss in the previous exposure (Phizackerley *et al.*, 1986). This compensation was quite effective at mitigating detector saturation by single large reflections, which could account for as much as 10% of the total counts collected during a frame.

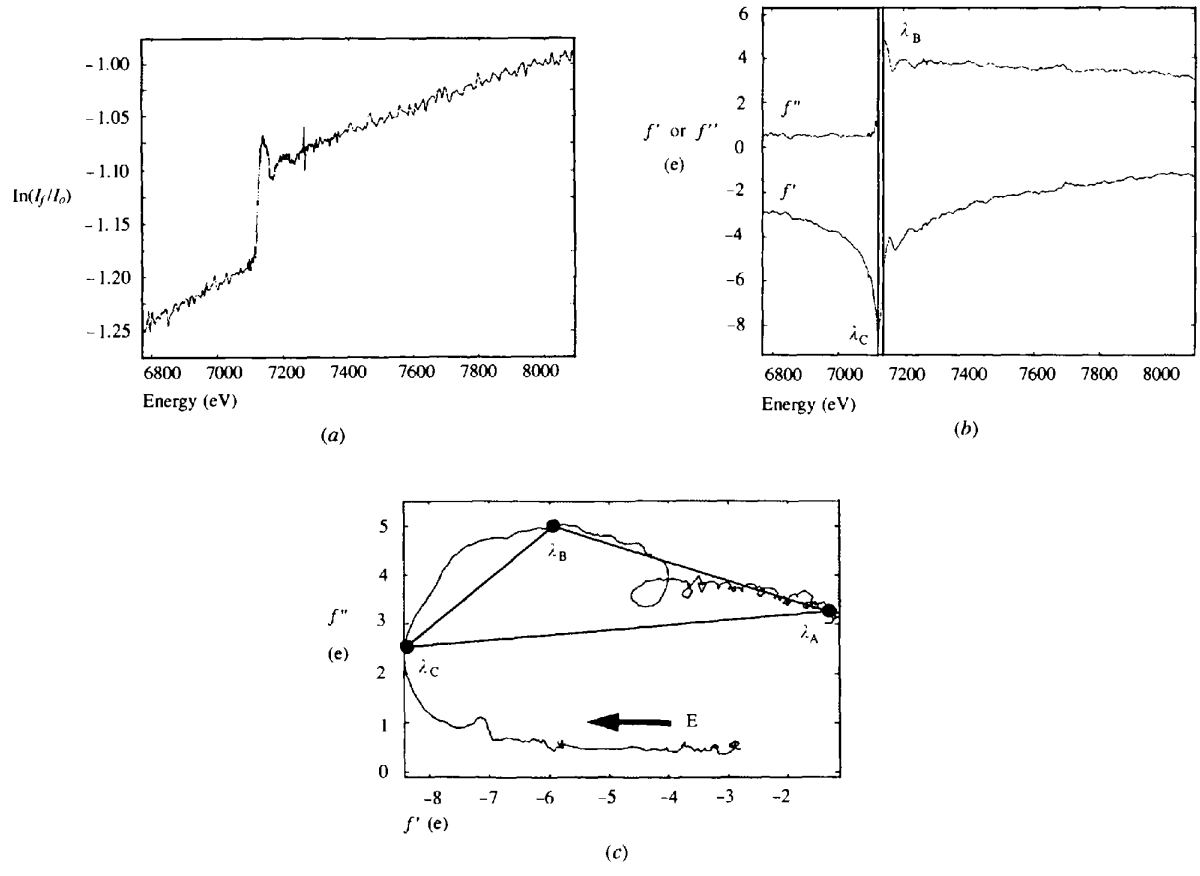

Fig. 1. Determination of the resonance scattering vector components of SiRHP crystals at the hemoprotein Fe K absorption edge. X-ray fluorescence scans (recorded with a scintillation counter) were taken between 6770.0 and 8091.90 eV with each reciprocal-space axis in the horizontal plane of the 95% horizontally polarized synchrotron beam. At each orientation, eight scans were performed for each of four different scanning intervals and energy ranges (6770.0–7089.5 eV, ΔE = 5 eV; 7090.25–7154.35 eV, ΔE = 0.4 eV; 7156.52–7378.56 eV, ΔE = 2 eV; 7384.35–8091.90 eV, ΔE = 5 eV). The smallest energy increment was necessary to define the edge, while the coarser increments used at pre- and post-edge regions were sufficient to allow extrapolation of the energy dependence of background absorption. Edge positions and scattering factors were calculated with *DISCO* (Eichhorn, 1985). (*a*) Dependence of SiRHP absorption with energy. The crystal is oriented with reciprocal-space axis b^* in the electric vector's plane of polarization. The linear absorption coefficient (μ) is directly proportional to ln(I_f/I_o), where I_f is the fluorescence intensity and I_o is the incident intensity. After the multiple fluorescence scans were merged, a polynomial was fit to the pre-edge region and then extended throughout the scan range. The polynomial fit values were subtracted from the data to remove the effects of energy-dependent changes in detector efficiency. Values of μ in the remote post-edge region were then used to scale the edge-jump to the theoretical value for Fe atom. (*b*) Dependence of f'' and f' with energy. f'' is proportional to μ and the photon energy (E). $f''(E) = (mcE\mu)/4\pi e^2\hbar$, where m is the electron mass, e its charge, c the speed of light and E the photon energy. f' is obtained from f'' by the Kramers–Kronig transformation (James, 1965), $f'(E) = 2/\pi \int[(E'f''/E^2 - (E')^2]dE'$. (*c*) Plot of f'' *versus* f' with energy increasing in the clockwise direction. The anomalous diffraction strength available in the experiment is related to the horizontal separation of the chosen collection energies and their vertical displacement from zero. E_B (7135.9 eV) and E_C (7120.4 eV) were chosen to maximize the magnitudes of f'' and f', respectively. The data in (*b*) and (*c*) were smoothed by averaging five adjacent points to reduce statistical fluctuations.

Table 1. *Comparison of observed and refined atomic anomalous scattering factors for different orientations of the SiRHP crystal*

X-ray fluorescence was measured for SiRHP crystals oriented with each principal reciprocal-space axis in the horizontal polarization plane of the synchrotron ring (see Fig. 1). The diffractometer geometry at beamline I-5AD prevented optimum positioning of the scintillation counter to record fluorescence with c^* in the horizontal axis, and as a result these scans were highly variable. (c^* corresponds to the long dimension of the SiRHP crystals that tends to lie along the capillary axis.) All orientations with a principal reciprocal-space axis in the horizontal gave nearly identical edge positions at the minimum of f': 7120.4 eV for a^*, 7119.6 eV for b^*, and 7120.9 eV for c^*. The width of the f' peak at half height is ~10 eV. Refined scattering factors from diffraction data taken with the crystal in the c^* orientation were consistent with values found for other orientations. For each crystal orientation with a reciprocal-space axis in the horizontal plane of polarization, scattering-factor refinement was carried out against a well determined set of $|^{\circ}F_A|$, $^{\circ}\Delta\varphi$ and $|^{\circ}F_T|$ by *MADLSQ* (Weis *et al.*, 1991). This refinement procedure assumes only one type of anomalous scatterer and isotropic anomalous scattering factors. Isotropic anomalous scattering factors are a reasonable assumption considering the results of the fluorescence scans (and the degree of measurement error present in the experiment, as discussed below). Estimated standard deviations (e.s.d.'s) in refined parameters are given in parentheses.

a^* coincident with direction of electric vector polarization

	Energy (eV)	Wavelength (Å)	f' (e) Observed	f' (e) Refined (e.s.d.)	f'' (e) Observed	f'' (e) Refined (e.s.d.)
(*A*)	8041.1	1.5418	−1.299	−1.14 (0.04)	3.195	3.39 (0.06)
(*B*)	7135.9	1.7374	−6.025	−6.41 (0.04)	4.492	4.37 (0.06)
(*C*)	7120.4	1.7412	−8.264	−8.07 (0.04)	2.551	2.83 (0.06)

b^* coincident with direction of electric vector polarization

	Energy (eV)	Wavelength (Å)	f' (e) Observed	f' (e) Refined (e.s.d.)	f'' (e) Observed	f'' (e) Refined (e.s.d.)
(*A*)	8041.1	1.5418	−1.210	−1.13 (0.03)	3.091	2.69 (0.05)
(*B*)	7135.9	1.7374	−5.925	−6.28 (0.03)	4.976	4.90 (0.05)
(*C*)	7120.4	1.7412	−8.396	−8.14 (0.03)	2.549	2.44 (0.05)

c^* coincident with direction of electric vector polarization

	Energy (eV)	Wavelength (Å)	f' (e) Observed	f' (e) Refined (e.s.d.)	f'' (e) Observed	f'' (e) Refined (e.s.d.)
(*A*)	8041.1	1.5418		−1.15 (0.01)		3.27 (0.02)
(*B*)	7135.9	1.7374		−6.33 (0.01)		4.55 (0.02)
(*C*)	7120.4	1.7412		−8.10 (0.01)		2.74 (0.02)

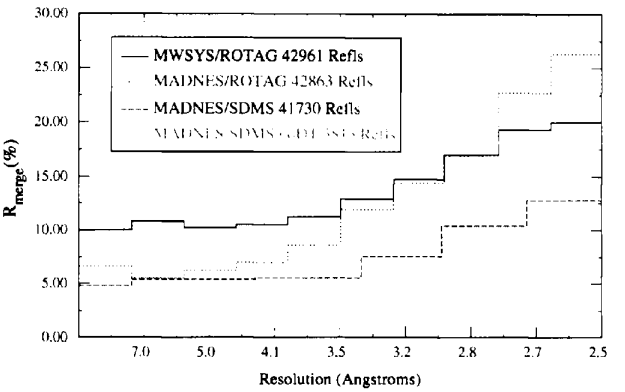

Fig. 2. Improvement in self-consistency for data collected at λ_A with different reduction and scaling approaches. R^I_{merge} is calculated in ranges of resolution (horizontal bars), plotted as a function of $(\sin\theta/\lambda)^2$, but expressed in Å. Data integrated with *MWSYS* [written by E. A. Merritt (Hendrickson, Pähler, Satow, Merritt & Phizackerley, 1989)], scaled with *ROTAVATA* (Collaborative Computational Project, Number 4, 1994), and purged of outliers by *AGROANO* (Weis, Kahn, Fourme, Driekamer & Hendrickson, 1991) have large discrepancies in the intensities of symmetry-equivalent reflections (*MWSYS/ROTAG*). Data integrated with *MADNES* (Messerschmidt & Pflugrath, 1987), with dead time, Lorentz, polarization, and absorption correction applied from *MWSYS*, scaled with *ROTAVATA*, and purged of outliers by *AGROANO* (*MADNES/ROTAG*), have lower R^I_{merge} values at medium and low resolution than *MWSYS/ROTAG*. *MADNES* integrated data scaled and purged of outlying measurements by San Diego Multiwire Software (Howard, Nielsen & Xuong, 1985). (*MADNES/SDMS*) are much more self-consistent in all resolution ranges. Two data runs (7385 reflections) through 18.5 and 14.8° of oscillation angle were discarded in *MADNES/SDMS* as they did not scale well with the rest of the data; both sections of crystal were previously exposed to X-rays. Of the remaining observations, many fewer were rejected by manual editing with *MADNES/SDMS* (652) than by *AGROANO* (2620), when a cutoff was set in *AGROANO* to reject reflections if $(I_{ih} - \langle I_h \rangle)/\sigma_h > 4.0$, where σ_h is derived from the distribution of measurements i for reflection **h**. Collecting data without altering the oscillation angle scan rate to compensate for dead-time event loss (*MADNES/SDMS* noDT) results in considerably higher R^I_{merge} values. Statistics for λ_B and λ_C show identical trends.

Exposure times were normalized by the dose (total counts) received in a N_2/He ion chamber to correct for time-dependent attenuation of the synchrotron beam. The variation in ion-chamber counts with ring current was monitored and found to be linear. Detector count rates varied between 17 and 30 kHz for the Fe wavelengths and 27 and 40 kHz for the Cu $K\alpha$ wavelength. The radiation doses to be received at each wavelength by a given crystal were normalized on specific individual reflection intensities prior to collecting each swath of data. Generally the λ_B and λ_C exposure times were 1.7 times longer than for λ_A to compensate for the less intense and more absorption-sensitive longer wavelengths. Depending on synchrotron ring current and crystal size, exposure times varied between 60 and 90 s per frame for λ_A, and 80 and 110 s per frame for λ_B and λ_C. Given SiRHP diffraction spot widths (0.2–0.8°), 0.1° oscillations were collected in 0.005° steps to optimize average intensity-to-background ratios. To further minimize background, beamline slits were adjusted between 0.5 and 0.8 mm in both horizontal and vertical directions to be commensurate with crystal orientation and size (typically 1.0 × 0.20 × 0.15 mm).

The data-collection strategy attempted to maximize resolution, exposure time, coverage of reciprocal space, and concomitant collection of Bijvoet pairs, given instrument contingencies and the allocated beamtime. Five crystals provided nine sections that were independently exposed to X-rays for data acquisition. At 4°, each section of the crystal typically lasted 48–60 h in the synchrotron beam before comparison of original and recollected frames indicated that high-resolution data were being lost. For each of three data-collection runs, crystal orientations were chosen so that a different principal crystallographic axis was parallel to the rotation axis. With these orientations, SiRHP crystal symmetry ($P2_12_12_1$) permitted simultaneous collection of Bijvoet pairs across the three orthogonal reciprocal-space mirror planes, thereby minimizing instrumentation, absorption or crystal decay-related systematic errors that might degrade phase information contained in the Bijvoet differences. The detector was placed 450 mm from the crystal (with a 355 mm long helium cone to limit air absorption) with a vertical 2θ swing of 24° for all data-collection runs. In this geometry, the detector subtends 35° of the Ewald sphere, and includes data between 13.5 and 2.5 Å resolution at the Fe energies, and between 13.5 and 2.2 Å resolution at Cu $K\alpha$. To fill in reciprocal space missed by the three orthogonal crystal orientations, four diagonal swaths were taken by setting χ to 45° and ratcheting φ (Xuong, Nielsen, Hamlin & Anderson, 1985). With $\chi = 45°$, Bijvoet pairs could not be collected concurrently; however, true inverse Friedel mates could be obtained by setting $\varphi' = \varphi + 180°$, setting $\chi' = -\chi$ and then collecting over the same range of ω. Time limitations restricted use of this data-collection strategy, allowing only two 25° inverse Friedel runs at λ_B to be collected. The Friedel mates that were missed unfortunately limited the number and quality of MAD phases that could be derived from the data set.

Table 2. *Identification and removal of a small number of misindexed reflections was the key to improving reduced diffraction data*

Reflection intensities for two reflections, $hkl = 1, 18, 6$ and $hkl = 3, 5, 15$ each with an aberrant measurement, are shown from different regions of reciprocal space where independent scale factors were assigned (scaling bins). Overlaps along the shortest reciprocal-space axis (c^*) from especially large neighboring reflections occasionally erroneously dominated the integration of weaker neighbors (values indicated with an asterisk). For $hkl = 1, 18, 6$, neighboring reflection $hkl = 1, 18, 5$ had an intensity of 4761 and was < 1 pixel away from $hkl = 1, 18, 6$ on the detector face; likewise for $hkl = 3, 5, 15$, nearby $hkl = 3, 5, 14$ was also large, having an intensity of 4246. These large outliers skewed automatic rejection algorithms and perturbed relative scale factors between shifts.

			Scaling bin	Intensity	σI
1	18	6	2404	1427.44*	228.67*
			2412	148.26	21.34
			4108	174.79	29.96
−1	−18	−6	2404	127.94	24.18
			2412	187.57	26.96
3	5	15	2304	3235.46*	216.26*
			2416	236.45	23.65
			4116	132.99	28.26
−3	−5	−15	2304	229.43	22.63
			2416	258.99	20.10

2.2. *Data reduction*

Time and instrumentation limitations forced a data-collection strategy that maximized resolution and coverage of reciprocal space, but resulted in data that were difficult to reduce and scale. The crystal-to-detector distance of 450 mm did not sufficiently separate the largest reflections from their neighbors on the detector face. This, combined with crystal slippage during data collection and inaccurate diffractometer parameters, complicated data processing. In the worst case of crystal slippage, the refined crystal orientation angles changed by more than 6° over a 25° data-collection run. In another instance, one run had to be broken into two parts when the orientation angles abruptly changed by ~3° in the rotation axis (SiRHP crystals are needles that tend to lie along the capillary). The data were initially manually indexed and reduced with the *MWSYS* software package developed by E. A. Merritt for use at beamline I-5AD (Hendrickson, Pähler, Satow, Merritt & Phizackerley, 1989) and internally scaled in 4° intervals of oscillation angle with *ROTAVATA* (Collaborative Computational Project, Number 4, 1994) and *AGROANO* (Weis *et al.*, 1991). *AGROANO* is a modified version of *AGROVATA* (Collaborative Computational Project, Number 4, 1994) that rejects outliers relative to redundant copies of the same Friedel mate (I^+ or I^-), as opposed to the average ($I^\pm$). Misindexing resulted from the inability to accurately

refine crystal parameters and missetting angles during spot integration coupled with the migration of integration boxes into large neighboring reflections (Table 2). Data reprocessing using *MADNES* (Messerschmidt & Pflugrath, 1987) with dead time, absorption, and polarization corrections applied from *MWSYS*, followed by profile fitting with *PROCOR* (Kabsch, 1988) and scaling with *ROTAVATA/AGROANO*, improved the consistency of symmetry-related reflection intensities as measured by $R^I_{\rm merge}$ values (Fig. 2). $R^I_{\rm merge} = \sum_{\rm h}\sum_i |I_{{\rm h}i} - \langle I_{\rm h}\rangle| / \sum_{\rm h}\sum_i |I_{{\rm h}i}|$, where $I_{{\rm h}i}$ is an individual intensity measurement and $\langle I_{\rm h}\rangle$ is the measurement average. Unfortunately, correlation coefficients calculated between observed and expected spot profiles were low (0.3–0.6) and anomalous signals were small, as judged by anomalous difference Patterson maps (Fig. 3) and diffraction ratios (Fig. 4). Normalizing each frame by the intensity of the background scattering in the water ring, a procedure highly effective in improving data collected on basic blue protein at beamline 1-5AD (Guss *et al.*, 1988) made little difference in the overall $R^I_{\rm merge}$ or anomalous signals for SiRHP data.

Large squared $(R^I_{\rm merge})^2$ values $(\sum_{\rm h}\sum_i |I_{{\rm h}i} - \langle I_{\rm h}\rangle|^2 \div \sum_{\rm h}\sum_i |I_{{\rm h}i}|^2)$ and inspection of *AGROANO* rejected reflections suggested that a few outliers were perturbing scale factors and falsely guiding automated reflection rejections. *MADNES*-processed data (summed intensities only, no profile fitting) were scaled in 5° swaths of oscillation angle with iterative single parameter scaling as implemented in the San Diego Multiwire Software (SDMS) (Howard, Nielsen & Xuong, 1985). Systematically scaling data sets from each of the nine crystal sections (over five crystals) against one another identified two deviant runs that were discarded. Both had been collected on a crystal position that had been previously exposed to X-rays. Sets of symmetry-equivalent measurements with large internal discrepancies were scrutinized visually to identify large, essentially misindexed measurements (see Table 2), the removal of which greatly decreased $R^I_{\rm merge}$ (Fig. 2), improved Bijvoet difference Patterson maps (Fig. 3) and anomalous diffraction ratios (Fig. 4). These overlapped, misindexed measurements not only inflated statistical assessments of precision, but also affected the scale factors between sections of reciprocal space covered by 5° swaths of oscillation angle. Interestingly, SDMS single parameter scaling proved more stable to these outliers than the second derivative least-squares protocol (Fox & Holmes, 1966) in *ROTAVATA* (Collaborative Computational Project, Number 4, 1994). SDMS application of rejections between successive scaling iterations was more effective than the *AGROANO* strategy of applying rejections only once, after scale

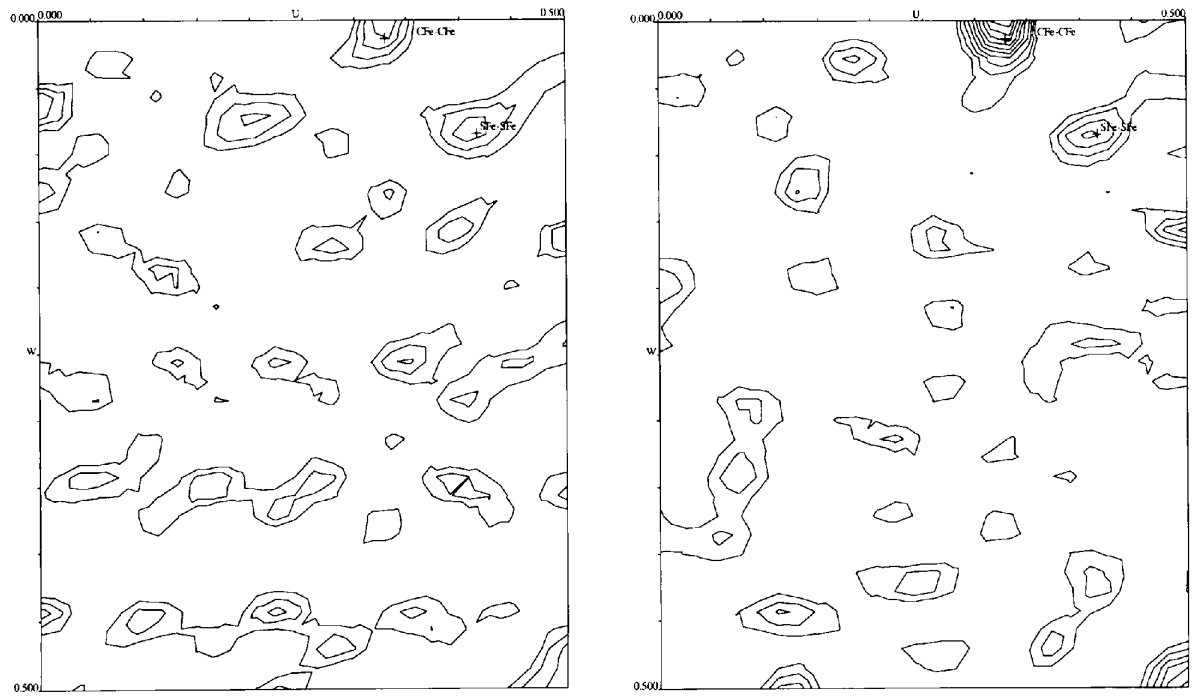

Fig. 3. Improvements of the anomalous signal in Bijvoet difference Patterson maps after data reprocessing. Bijvoet difference Patterson maps show the improvement of anomalous signals between (*a*) the original *MWSYS/ROTAG* processed data, and (*b*) the final *MADNES/SDMS* processed data. Maps are calculated with $[|F^+(\lambda_B)|^2 - |F^-(\lambda_B)|^2]$ coefficients from diffraction data between 12.0 and 4.0 Å resolution collected at λ_B. The positions of self-peaks for the siroheme Fe atom (SFe) and Fe_4S_4 cluster center (CFe) from the the final 1.6 Å resolution refined model are shown on the $V = 0.5$ Harker section. Maps are contoured in intervals of σ, beginning at 1σ.

factors have converged in *ROTAVATA*. Scale factors (g_i) assigned to separate sections of reciprocal space (scaling bins, i) attempt to minimize the sum of the residuals (Ψ) between symmetry-related intensities ($I_{\mathbf{h}i}$) of reflection **h**.

$$\Psi = \sum_{\mathbf{h}} \sum_{i} [w_{\mathbf{h}i}(g_i\langle I_{\mathbf{h}}\rangle - I_{\mathbf{h}i})]^2. \quad (1)$$

where $w_{\mathbf{h}i}$ represents a relative weighting factor for $I_{\mathbf{h}i}$ and $\langle I_{\mathbf{h}}\rangle$ is the measurement mean. SDMS uses iterative linear least-squares to alternately solve for $\langle I_{\mathbf{h}}\rangle$ with g_i fixed, and then g_i with $\langle I_{\mathbf{h}}\rangle$ fixed (Howard *et al.*, 1985; Monahan, Schiffer & Schiffer, 1967). In contrast, *ROTAVATA* applies a non-linear least-squares approach that assumes a linear, truncated Taylor expansion to minimize Ψ directly in terms of g_i (Fox & Holmes, 1966)

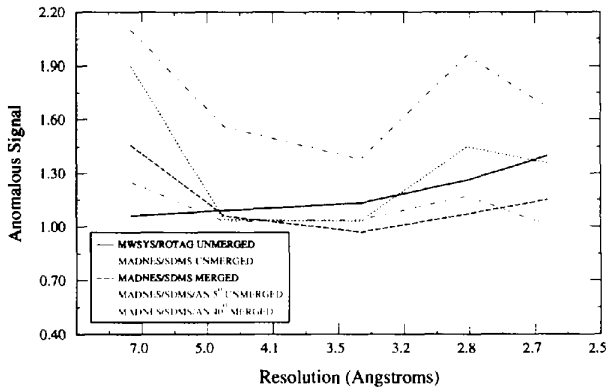

Fig. 4. Improvement of anomalous difference diffraction ratios at λ_A by local anisotropic scaling and not merging redundant measurements. When redundant measurements were not merged to an asymmetric unit, *MADNES* processed data that were scaled and purged of outliers with *SDMS* (*MADNES/SDMS* UNMERGED) show a substantial gain in signal at both high and low resolution compared to *MWSYS* processed data scaled with *ROTAVATA* and purged of outliers with *AGROANO* (*MWSYS/ROTAG* UNMERGED). Merging redundant measurements within the *MADNES/SDMS* treated data attenuated the anomalous signal (*MADNES/SDMS* MERGED). Local anisotropic scaling of *MADNES/SDMS* data significantly improved anomalous signals (*MADNES/SDMS/AN*) only when the data were scaled locally in small 5° swaths of oscillation angle. Anisotropic scaling within reciprocal-space sections that were merged across 40° of oscillation angle produced a negligible signal, reflecting variability of average diffraction over relatively short time periods and small ranges of reciprocal space. Anomalous signal is given as the ratio of anomalous diffraction ratios [r.m.s.$(|F^+| - |F^-|)$/r.m.s.$|F|$, r.m.s. = root mean square] between the acentric and centric reflections [plotted as a function $(\sin\theta/\lambda)^2$, but expressed in Å]. For data merged to an asymmetric unit, the merged acentric values are given relative to the unmerged centric values. Local scaling within oscillation wedges of reciprocal space was performed with *ANOSCL* (Hendrickson, 1988) which minimizes $\sum_h (K - |F^+|/|F^-|)^2$, where K is an anisotropic scale expressed in the orthogonal coordinate system of a, c^* and ac^*. Statistics were compiled over the resolution bins (13.5–6.0, 6.0–4.0, 4.0–3.0, 3.0–2.8, 2.8–2.5 Å) with the diffraction-ratio values plotted at the middle of the resolution range.

The SDMS algorithms were more stable to large deviant measurements and the ability to visually edit reflection sets allowed these large outliers to be identified and removed early in the scaling process. This treatment led to the first encouraging anomalous difference Patterson maps (Fig. 3).

Final data-reduction statistics emphasize low redundancy and an observed anomalous signal that is comparable to the errors between symmetry-related reflections (R^F_{merge}) (Table 3). Unfortunately, all measurements of $|F^+|$ are not matched by an associated measurement of $|F^-|$ because Bijvoet pairs could not be collected concurrently for orientations where a principal crystal axis did not fall in the plane perpendicular to the rotation axis. With weak data, low redundancy can result in poor amplitude estimates, while incomplete Bijvoet pairs reduce the number of observations that contribute to determining the local phasing parameters for a given reflection.

Merging redundant observations of a given reflection was generally detrimental to the anomalous signals (Fig. 4). Even when redundant measurements were only merged within wedges of reciprocal space delimited by 40° in oscillation angle, most of the anomalous difference signal between Bijvoet pairs was lost (Fig. 4). Anisotropic local scaling (*ANOSCL*, Hendrickson, Smith, Phizackerley & Merritt, 1988) of unmerged reflections within wedges of reciprocal space delimited by 5° in oscillation angle greatly increased the anomalous difference signal between acentric Bijvoet pairs. Anisotropic local scaling within 40° wedges of reciprocal space did little to improve the signal. Data collected at different wavelengths were scaled to each other anisotropically by least squares, as implemented in the program *WVLSCL* (Hendrickson *et al.*, 1988). Despite the improvement in signal, treatment of the data in small local swaths for scaling and phase extraction further limits the number of unique $|F^+|$ and $|F^-|$ pairs that can be combined.

3. Results

3.1. *Determination and refinement of the anomalous scattering model*

Large observational errors in anomalous differences and incompleteness of unique data caused refinement of the anomalous scattering model to converge with inaccurate Fe positions, which ultimately lead to poor phase estimates. The anomalous scatterers were initially modeled as a siroheme Fe and a single 'super-atom' with occupancy four, representing the Fe_4S_4 cluster. This model was initially fit to a Bijvoet difference cross-Fourier map calculated with amplitudes from the wavelength B $[|F^+(\lambda_B)| - |F^-(\lambda_B)|]$ and phased with adjusted MIR phases ($\varphi_{\text{MIR}} - \pi/2$) to produce the imaginary Fourier summation (Kraut, 1968). The handedness of the

Table 3. *Statistical summary of MAD data before local scaling*

Completeness of unique data measured to 2.5 Å resolution is less for $|F^-|$ than for $|F^+|$ because Friedel mates were only measured for some of the data-collection runs where a principal crystal axis was not perpendicular to the rotation axis. The completeness and redundancy for λ_B is greater than for λ_C because inverse Friedel mates were collected at $\chi = 45°$, for 46.1° of ω, only at λ_B. R^F_{merge} is given in terms of structure-factor amplitudes, rather than intensities, for direct comparison with the calculated and observed signals. $R^F_{\text{merge}} = \sum_{\mathbf{h}} \sum_i |\,|F^{\pm}_{\mathbf{h}i}| - \langle|F^{\pm}_{\mathbf{h}}|\rangle\,| / \sum_{\mathbf{h}} \sum_i |F^{\pm}_{\mathbf{h}i}|$. Calculated Bijvoet signal $= q(2f'')$, where $q = (N_a/2N_p)^{1/2}(1/Z_{\text{eff}})$. N_a is the number of anomalous scattering centers, N_p, the number of non-H enzyme atoms (4011 for SiRHP) and Z_{eff}, the effective normal scattering factor for an average protein atom (~6.62 e). Observed Bijvoet signal = r.m.s.$(\Delta|F^{\pm}_{\mathbf{h}}|)$/r.m.s.$(|F_{\mathbf{h}}|)$. The observed signals are larger than those calculated due to correlated scattering at lower resolution from the neighboring Fe atoms [an increase of $\sim (N_a)^{1/2}$, and lower attenuation of observable anomalous scattering with higher resolution, compared with normal scattering]. Errors estimated from symmetry-equivalent centric reflections are given in parentheses. Calculated dispersive signal $= q[f'(\lambda_i) - f'(\lambda_j)]$. Observed dispersive signal = r.m.s.$(\Delta|F^{\Delta\lambda}_{\mathbf{h}}|)$/r.m.s.$(|F_{\mathbf{h}}|)$.

	Wavelength (Å)	Completeness $\|F^+\|$ (%)	Completeness $\|F^-\|$ (%)	Redundancy $\|F^+\|$ (%)	Redundancy $\|F^-\|$ (%)	R^F_{merge} on $\|F^{\pm}\|$ (%)	Bijvoet signal Obs. (%)	Bijvoet signal Calc. (%)	Dispersive signal Obs. (%)	Dispersive signal Calc. (%)
(*A*)	1.5418	93.0	74.7	1.5	1.4	5.6	5.7 (1.7)	1.9	(*versus B*) 3.5	(*versus B*) 1.8
(*B*)	1.7374	91.4	74.7	1.7	1.5	6.2	6.5 (1.5)	3.6	(*versus C*) 4.3	(*versus C*) 0.9
(*C*)	1.7412	90.0	68.7	1.4	1.3	5.3	5.7 (1.7)	2.4	(*versus A*) 5.2	(*versus A*) 2.7

MIR derivatives imposed the correct configuration on the Fe model. These positions were then refined against normal scattering-factor amplitudes of the anomalously scattering atoms ($|{}^\circ F_A|$) extracted from the resonance scattering equations by the least-squares treatment of *MADLSQ* (Hendrickson *et al.*, 1988) (Table 4).

In the *MADLSQ* procedure, at least four independent restraints on each reflection (that is, four observations of different Bijvoet mates at different wavelengths) are necessary to determine a system of equations linear in the wavelength-independent parameters $|{}^\circ F_A|^2$, $|{}^\circ F_T|^2$ (squared normal scattering amplitude of all atoms in the unit cell), and the cosine and sine of the phase difference between ${}^\circ F_T$ and ${}^\circ F_A$ (${}^\circ\varphi_T - {}^\circ\varphi_A$) scaled by $|{}^\circ F_A||{}^\circ F_T|$ (Table 4).

$$|F^{\pm}(\lambda)|^2 = |{}^\circ F_T|^2 + a(\lambda)|{}^\circ F_A|^2 + b(\lambda)|{}^\circ F_T||{}^\circ F_A|\cos({}^\circ\varphi_T - {}^\circ\varphi_A) \pm c(\lambda)|{}^\circ F_T||{}^\circ F_A|\sin({}^\circ\varphi_T - {}^\circ\varphi_A), \quad (2)$$

where for the wavelength-dependent terms,

$$a(\lambda) = [(f')^2 + (f'')^2]/(f^\circ)^2 \quad (3)$$

$$b(\lambda) = 2(f'/f^\circ) \quad (4)$$

$$c(\lambda) = 2(f''/f^\circ). \quad (5)$$

f° represents the normal atomic scattering factor for the anomalously scattering atoms, and f' and f'' are orthogonal components of the atomic anomalous-scattering factor. Comparison of the $|{}^\circ F_A|$ distribution generated in *MADLSQ* with the theoretical distribution calculated from the estimated Fe-atom positions indicated that measurement error coupled with poorly restrained least-squares equations can produce unrealistic $|{}^\circ F_A|$ values (Fig. 5). The quality of $|{}^\circ F_A|$ Patterson maps (Fig. 6) increased substantially if the threshold for excluding large $|{}^\circ F_A|$ values was set to 280 e, lower than was suggested by the maximum value of 330 e derived from the theoretical distribution of $|{}^\circ F_A|$ values (Fig. 5). This indicates that the distribution of unreasonably large $|{}^\circ F_A|$ values determined experimentally overlaps with the theoretical distribution. The removal of aberrant parameter estimates is critical for generation of Patterson map coefficients and refinement of the anomalous scattering model. Refinement of the heme and super-atom Fe atom positions against the *MADLSQ* derived $|{}^\circ F_A|$ was carried out in *X-PLOR* (Brünger, Kuriyan & Karplus, 1987) using Powell conjugate-gradient minimization (Powell, 1977). (Refinement against 7985 reflections to 2.5 Å res-

Table 4. *MADLSQ phasing statistics for reflections with ≥ 4 observational restraints*

$\langle|{}^\circ F_T|\rangle$ is the average value of the normal-scattering structure-factor amplitudes determined from 14 541 acentric and 2323 centric reflections by *MADLSQ*, whereas $\langle|{}^\circ F_A|\rangle$ is the average value of the normal-scattering structure-factor amplitudes for atoms that also scatter anomalously. The standard deviations (σ) in $|{}^\circ F_T|$, $|{}^\circ F_A|$ and $\varphi_T - \varphi_A$, derived from the least-squares fit of each local parameter set, are averaged over all reflections. The relatively large values of $\sigma|{}^\circ F_A|$ compared to $\langle|{}^\circ F_A|\rangle$ reflect the difficulty in refining the SiRHP anomalous scatterer model against the *MADLSQ* $|{}^\circ F_A|$ estimates. The values for $\langle|{}^\circ F_A|\rangle$ are approximately twice as large as would be expected from SiRHP's Fe atoms [26 electrons × $(20\text{Fe})^{1/2} = 116$], thus indicating the presence of anomalously large estimates for $|{}^\circ F_A|$. The average closure for *MADLSQ* least-squares fitting of individual reflections (Q) is 10.9, where $Q = \langle\{\sum[|F^{\pm}(\lambda)|_{\text{obs}} - |F^{\pm}(\lambda)|_{\text{calc}}]^2/N_{\text{obs}}\}^{1/2}\rangle$ and N_{obs} is the number of independent observations in phasing a given reflection by least squares. Of 16 865 reflections with ≥ 4 independent observations, 3667 were rejected as they produced estimates of $|{}^\circ F_A| \le 0$ or $|{}^\circ F_A| \ge 750.0$ (see Fig. 5), 666 were rejected for $|{}^\circ F_T| \le \sigma|{}^\circ F_T|$ or $|{}^\circ F_A| \le \sigma|{}^\circ F_A|$, 2234 were rejected for $Q \ge 20.0$, and 35 were rejected for $\sigma\varphi \ge 70.0$. Probability distributions were determined for the remaining 10 263 reflections with *MADABCD* (Pähler, Smith & Hendrickson, 1990), and then redundant reflections were merged (by summing exponential ABCD coefficients) with *MERGUR* (Yang, Hendrickson, Crouch & Satow, 1990) leaving 8058 unique reflections. On comparison of parameters from redundant reflections prior to merging: $R(|{}^\circ F_T|) = 0.095$, $R(|{}^\circ F_A|) = 0.579$, and $\langle\Delta({}^\circ\varphi_T - {}^\circ\varphi_A)\rangle = 53.8°$. After combining phase distributions $\langle|{}^\circ\varphi_T(\text{combined}) - {}^\circ\varphi_T(i)|\rangle = 29.5°$, where i is one in a set of redundant reflections. Less stringent cutoffs were explored, but produced experimental electron-density maps of undistinguished quality at best.

	Obs.	$\langle\|{}^\circ F_T\|\rangle$	$\langle\sigma\|{}^\circ F_T\|\rangle$	$\langle\|{}^\circ F_A\|\rangle$	$\langle\sigma\|{}^\circ F_A\|\rangle$	$\langle\sigma({}^\circ\varphi_T - {}^\circ\varphi_A)\rangle$
Acentric	14541	472.0	20.7	257.8	61.0	24.3
Centric	2323	470.0	27.5	259.6	84.8	

olution converged with an R factor = 51.8%.) Refinement of the anomalous scattering model against the strongest set of Bijvoet differences (taken at λ_B) was quite unstable. A systematic rotational search over the Euler angles of an idealized Fe_4S_4 cluster centered on the super-atom position was carried out to confirm the cluster orientation that resulted from the *X-PLOR* refinement. The search attempted to maximize a figure-of-merit (FOM) based on the lack-of-closure $[|F^{\pm}(\lambda)|^2_{obs} - |F^{\pm}(\lambda)|^2_{calc}]$ for (2), given *MADLSQ* determined parameters and $|^{\circ}F_A|$ values calculated from the Fe-atom positions (Fig. 7). Although a second subsequent *X-PLOR* refinement of a siroheme Fe and rigid Fe_4S_4 cluster (R factor = 48.9% at convergence) improved Fe-atom positions, they remained displaced from their 'true' values (taken as the coordinates in the refined 1.6 Å resolution SiRHP structure) by a 0.63 Å root-mean-square deviation (r.m.s.d.). The strong correlation observed between the displacement of the siroheme Fe atom and the cluster Fe atoms from their respective 'true' coordinates (Fig. 7) may result from the best determined $|^{\circ}F_A|$ values occurring in a resolution range (4.5–3.5 Å) that corresponds to the $Fe_{siroheme}$—Fe_4S_4 cluster separation (4.5 Å). In this resolution range, normal scattering begins to fall off relative to anomalous scattering, yet the anomalous differences have not yet degraded from lack of intensity at higher resolution. When the true cluster center was used in the rotational search, the correct cluster orientation produced the largest FOM (see legend to Fig. 7). Errors in the Fe-atom anomalous-scattering model did limit phase accuracy (see Table 5).

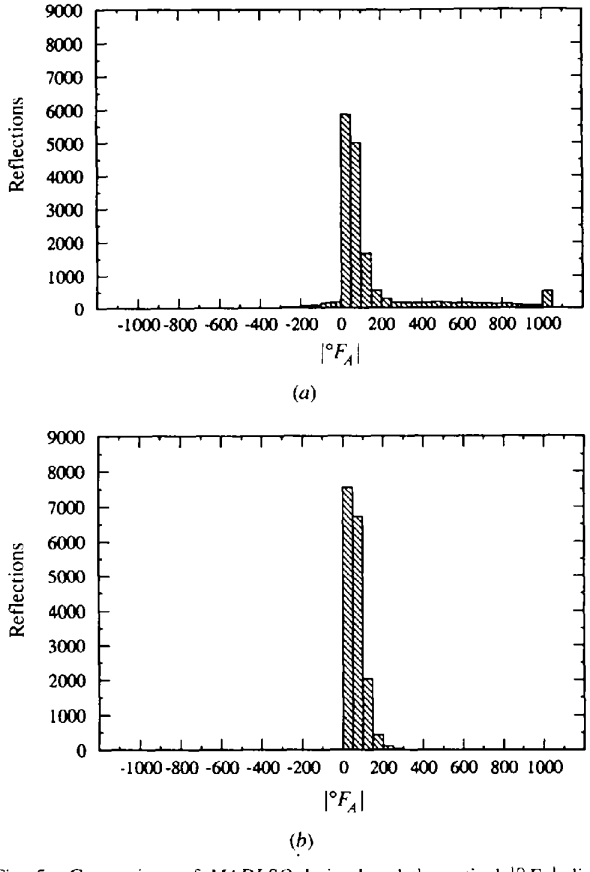

Fig. 5. Comparison of *MADLSQ*-derived and theoretical $|^{\circ}F_A|$ distributions. (*a*) Histogram of *MADLSQ*-derived $|^{\circ}F_A|$ values from reflections with ≥4 independent observations. (The 16 865 reflections are not reduced to an asymmetric unit.) $|^{\circ}F_A|$ is expressed in electrons (e) as the distribution of observed values has been scaled to the theoretical distribution shown below by a least-squares procedure described in the text. Each $|^{\circ}F_A|$ bin contains all values between $|^{\circ}F_A|$ and $(|^{\circ}F_A| - 50)$, except the bins beginning at ±1000 which contain all values with magnitudes greater than 1000. (*b*) Histogram of the theoretical $|^{\circ}F_A|$ values calculated for the reflections in (*a*) given the SiRHP Fe positions used in phase analysis. Although total correlated scattering from all 20 Fe atoms in the SiRHP unit cell could produce a maximum $|^{\circ}F_A|$ value of 520 e, the maximum theoretical value for the reflections observed is 330 e.

3.2. *MAD phase determination*

Phase determination from a MAD experiment, as from an MIR experiment, requires both reciprocal-space parameters local to a given reflection ($|^{\circ}F_T|$, $|^{\circ}F_A|$, $^{\circ}\varphi_T - ^{\circ}\varphi_A$) and global real-space parameters (Fe coordinates, thermal and occupancy factors), upon which otherwise unobtainable reciprocal-space parameters depend ($^{\circ}\varphi_A$). For SiRHP, in order to extract phases for a reflection with less than four phasing restraints (49% of the data to 2.5 Å), some local parameters had to be derived separately from the global anomalous scattering model. This model was previously determined from the local parameters of those reflections that were sufficiently restrained for estimation by *MADLSQ* (MAD 4, Table 5).

For the data with ≥4 restraints, phases were calculated with *MADABCD* (Pähler, Smith & Hendrickson, 1990). When provided with *MADLSQ* estimated local parameters and the anomalous scattering model, *MADABCD* weights all possible values of phase by a probability function based on the lack-of-closure for (2), thereby producing a centroid phase estimate. Surprisingly, this treatment was not more effective than simply calculating $^{\circ}\varphi_A$ from the anomalous-scattering model and adding it to the *MADLSQ*-determined $^{\circ}\varphi_T - ^{\circ}\varphi_A$ value (Table 5). When using the 'true' Fe-atom positions in the phase calculation, the map correlation coefficient R_c (see legend to Table 5) is actually better without using the probabilistic expression [$\Delta\varphi - ^{\circ}\varphi_A$ *versus* $P(^{\circ}\varphi_T)$, Table 5]. However, the *MADABCD* treatment cast the phase distributions in the form of Hendrickson–Lattman (*ABCD*) coefficients (Hendrickson & Lattman, 1970), which facilitated subsequent combination with MIR phasing information. Reflections with three phasing restraints could be phased by *MADLSQ* and *MADABCD* if the $|^{\circ}F_A|$ values were first calculated from the anomalous scattering model. Recursive

least-squares scaling between $|^{\circ}F_A|_{calc}$ values calculated from the anomalous scattering model and $|^{\circ}F_A|$ values determined from *MADLSQ* for sufficiently restrained reflections was used to place $|^{\circ}F_A|_{calc}$ values that could only be calculated from the anomalous scattering model on the same scale as the observed amplitudes. *MADLSQ* values that differed from the calculated values by an increasingly more stringent cutoff based on σF_A were discarded. Scale factors converged after six iterations with $||^{\circ}F_A|_{MADLSQ} - |^{\circ}F_A|_{calc}| \leq 2.5 \times \sigma F_A$. Reflecting indeterminacy, phase errors for reflections with fewer than four phasing restraints were higher than those for reflections with ≥ 4 restraints (Table 5). In order to integrate a lack-of-closure based probability distribution over a single variable of phase for reflections with only two phasing restraints, a prior estimate for $|^{\circ}F_T|$ as well as for $|^{\circ}F_A|$ must be obtained without using the least-squares treatment of *MADLSQ*. At set values of $(^{\circ}\varphi_T - {}^{\circ}\varphi_A)$ and $|^{\circ}F_A|$, (2) is a quadratic in $|^{\circ}F_T|$ that can be solved using one of two observations. (Although the quadratic provides two solutions for $|^{\circ}F_T|$, one is generally negative.) Thus, $|^{\circ}F_T|$ can be determined at all values of $(^{\circ}\varphi_T - {}^{\circ}\varphi_A)$ and evaluated for lack-of-closure of (2) with the remaining observation. Unfortunately, this treatment correlates the errors in the wavelength-independent parameters and contributes to the large phase distribution variances of reflections with only two observational restraints.

A simple attempt at modeling the MAD data analogously to MIR data produced worse phase estimates than the *MADLSQ/MADABCD* approach described above (Table 5). MIR and MAD phasing experiments are conceptually similar as both involve extracting phase information from amplitude variation dependent on a known perturbative scattering vector. Conventional MIR phasing methods can be applied to MAD data by treating intensities collected at one wavelength as a native data set with anomalous scattering, and intensities collected at the other wavelengths as derivative data sets with anomalous scattering. When implementing this approach, the SDMS-scaled data were reduced to an asymmetric unit (no local anisotropic scaling), and then using relative Wilson scaling in *PHASES*, λ_B and λ_C were scaled to the pseudo-native data set, λ_A. 'Isomorphous' differences corresponded to the dispersive differences [derived from $f'(\lambda_B) - f'(\lambda_A)$ and $f'(\lambda_C) - f'(\lambda_A)$], while the 'anomalous differences' corresponded to the Bijvoet differences of each wavelength [derived from $f''(\lambda)$]. {For 'isomorphous' phasing $|F_{Der}| \simeq [|F^+(\lambda_{B \text{ or } C})| + |F^-(\lambda_{B \text{ or } C})|]/2$ and $|F_{Nat}| \simeq [|F^+(\lambda_A)| + |F^-(\lambda_A)|]/2$.} Isomorphous or anomalous occupancies can act as scale factors for the

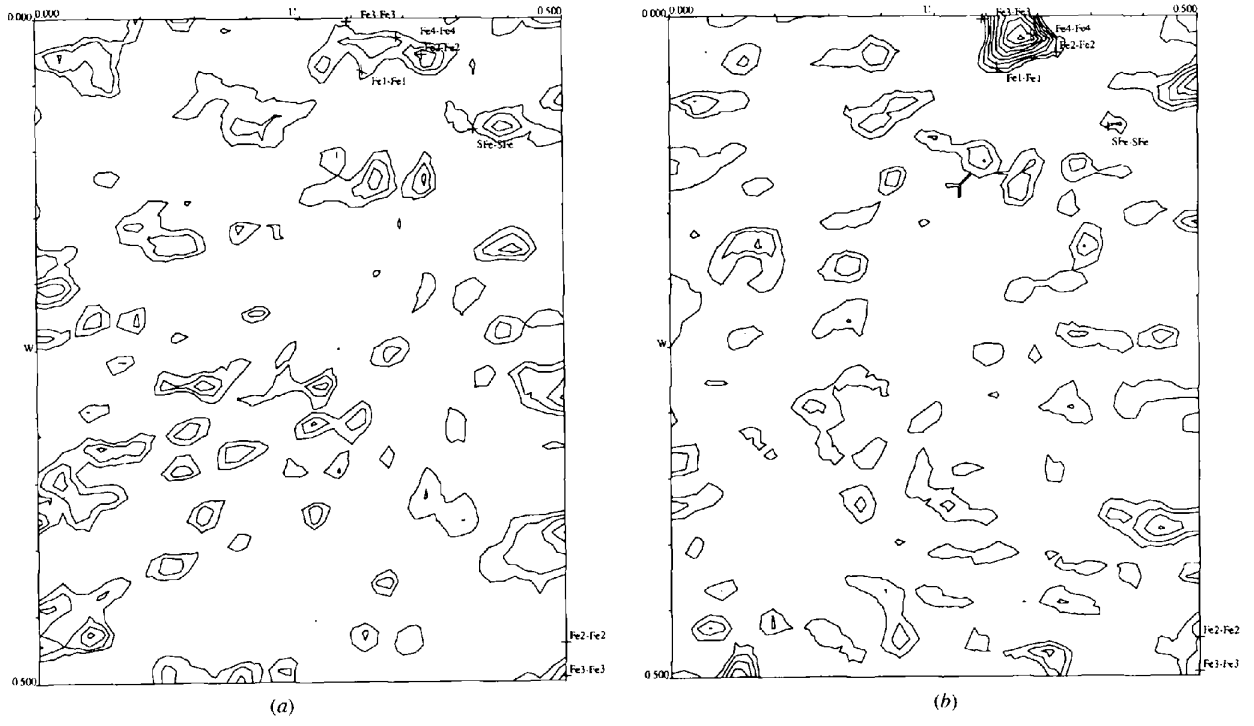

Fig. 6. Improvements in $|^{\circ}F_A|$ Patterson maps from the removal of large aberrant coefficients. (*a*) Patterson map calculated from 2.5 to 12.0 Å using *MADLSQ* derived $|^{\circ}F_A|$ values between 0 and 560 e. Predicted self peaks based on the final refined Fe-atom positions for the cluster (Fe1 to Fe4), the siroheme Fe atom (SFe) are shown on the $V = 0.5$ Harker section. 8970 $|^{\circ}F_A|$ values were used, representing 53.4% of the unique data. The map is contoured in increments of σ, beginning at 1σ. (*b*) Similar map as in (*a*) except that only $|^{\circ}F_A|$ values between 0 and 280 e were selected. 7985 $|^{\circ}F_A|$ values were used, representing 47.5% of the unique data.

$\Delta f'$ and f'' values. The limitations of this particular approach were that the data are merged before phasing so that local observations collected closely together in time and reciprocal space do not alone contribute to a given phase, and that the pseudo-native data set is weighted more heavily than the others.

3.3. *Combination of MAD with MIR phase information*

Combination of MAD phase information with MIR phase information substantially improved the quality of experimental electron-density maps (Fig. 8). MAD phase distributions from symmetry-related reflections, expressed in terms of Hendrickson–Lattman coefficients, were combined with each other by summing the exponential *ABCD* coefficients and reintegrating over all values of phase. The resulting MAD phases (overall completeness of 69% to 2.5 Å) were then used to more accurately estimate the isomorphous lack-of-closure errors in the MIR phase calculation [performed with modified versions of *PHASIT* from the *PHASES* package (Furey & Swaminathan, 1990)]. Before combining MAD and MIR *ABCD* coefficients, the phase distributions were weighted relative to each other by applying a multiplicative factor to the MIR *ABCD* coefficients, which could act to either inflate or deflate the MIR phase distribution variances. Although the electron-density maps derived from MAD phases alone or MIR phases alone have quite different features, the most interpretable combined map was obtained when the MAD and MIR phase sets were weighted equally (Fig. 8). Consistent with this, the MAD and MIR phase errors (compared to the refined model) are reasonably close in value (Table 5).

4. Discussion

Determining the structure of SiRHP by exploiting its relatively small Fe-atom anomalous signal was challenging given the available synchrotron source, instrumentation, and data analysis methodology. Since the time of the experiment, substantial improvements in all of these areas have made, and will continue to make, MAD more and more accessible to protein crystallographers. Still, many lessons were learned from our experience with SiRHP that are likely to be applicable to future experiments on other systems that also have less than ideal experimental parameters. SiRHP data reduction was complicated by crystal slippage, closely separated large reflections, marginal completeness and redundancy, and the sensitivity of non-linear least-squares scaling to outliers. These difficulties were eventually overcome by a progressively more manual and more scrutinizing approach to data processing. Although some of these problems were idiosyncratic, they do emphasize the overwhelming importance of being able to accurately

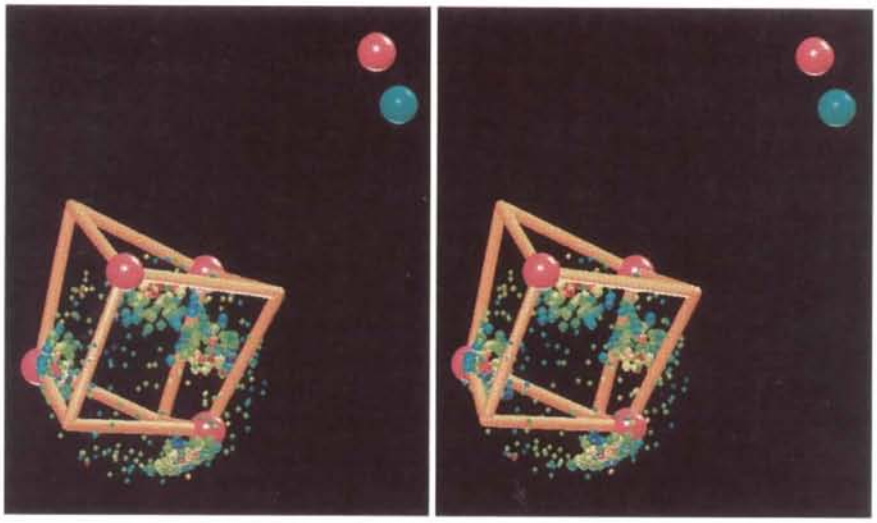

Fig. 7. Systematic rotational search of the Fe_4S_4 cluster to optimize overall lack-of-closure of the resonance scattering (2). The rotational search was carried out over the three Euler angles (X—Z—X) of an idealized Fe_4S_4 cluster centered on the position found by refinement of a 'super-atom' position against the *MADLSQ* derived $|^{\circ}F_A|$ values (see text). The Fe_4S_4 cluster Fe-atom positions from the 1.6 Å resolution SiRHP model (brown, cluster with gold bonds) are displaced from the center of the rotation search in the same direction as the siroheme Fe-atom position in the final model (brown) is from the position obtained by refinement against the anomalous data (cyan). Lack-of-closure of (2) was calculated for all MAD data at each cluster orientation and scored by the overall figure-of-merit (FOM) after the derived distributions were integrated over all values of phase. A coarse search over all rotational space was performed first using 30° intervals followed by finer searches of 5 and 2° around the maxima of preceding search. Small colored spheres represent the Fe atoms of every fifth cluster orientation sampled in the 30° search, while large colored spheres represent every fifth orientation of the 5° search. FOM increases from blue to green to yellow to red in the range from 0.489 to 0.534. The FOM calculated with Fe-atom positions taken from the 1.6 Å resolution refined model (FOM = 0.729) was higher than for any other configuration of the anomalous scattering model assessed. The figure was displayed by the *MV*102 molecular representation module written by T. J. Macke and rendered under the AVS environment (Upson *et al.*, 1986).

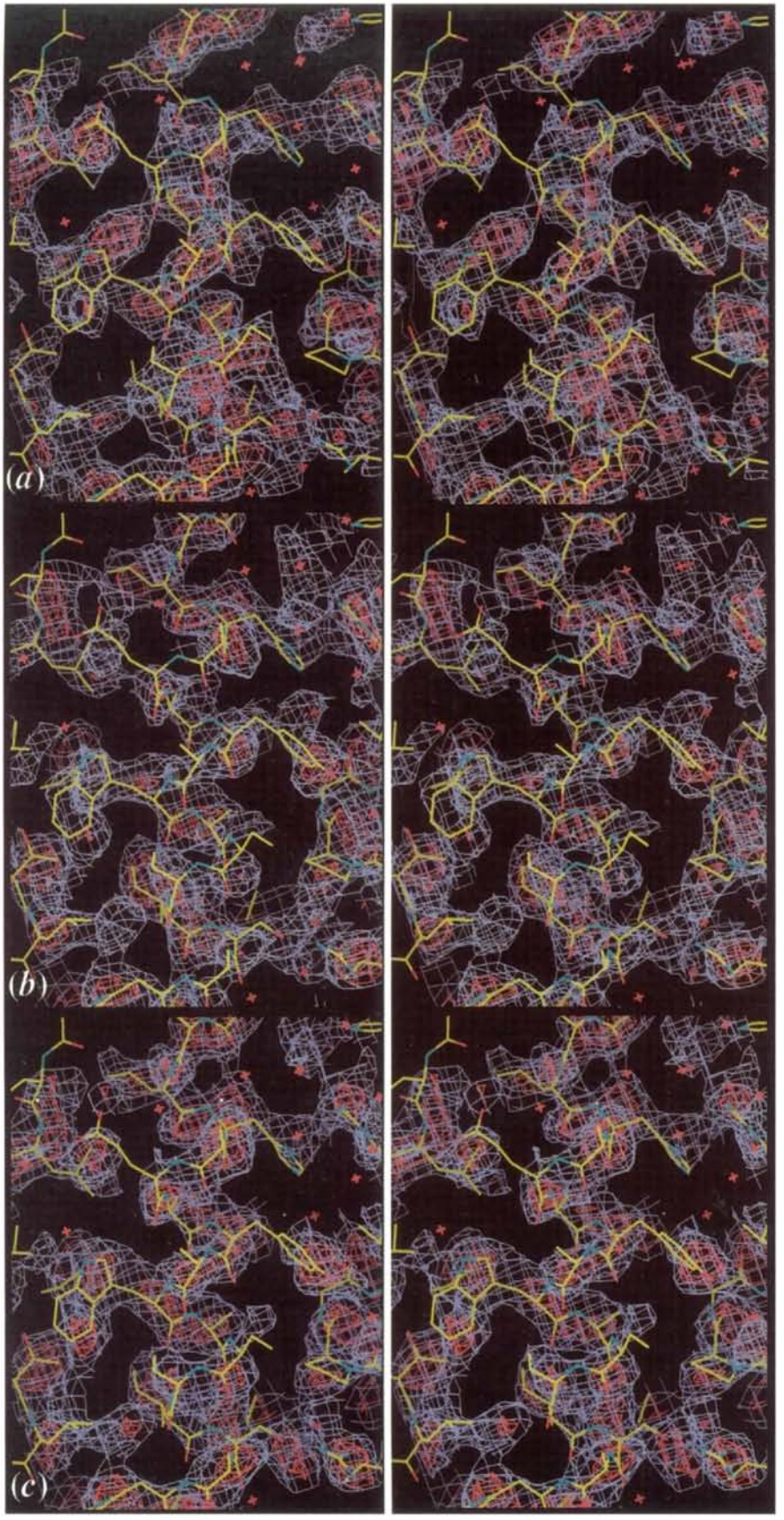

Fig. 8. Improvement in experimental electron-density maps on combination of MAD and MIR phase information. (*a*) MIR phased (Table 5) $|^{\circ}F_T| \times$ FOM electron-density map (30.0–2.5 Å resolution, purple contours at 1σ, red at 2σ). The tube of density matches the helix axis in the refined model (yellow C atoms, blue N atoms, red O atoms, water molecules shown as crosses), but peripheral detail is weak and there are false connections. (*b*) MAD phased (Table 5) $|^{\circ}F_T| \times$ FOM electron-density map (13.0–2.5 Å resolution). Although fine features appear to be more accurate than (*a*) the lack of low-resolution data and incompleteness result in choppiness and chain breaks. (*c*) MAD/MIR combined phased (Table 5) $|^{\circ}F_T| \times$ FOM electron-density map (30.0–2.5 Å resolution). Fine features are more interpretable, the density for the peptide backbone is now continuous at 2σ, and the chain breaks have been mostly eradicated. The figure was rendered with *XFIT* (McRee, 1992).

Table 5. *Average errors of MAD-derived and MAD/MIR combined phases*

Phase errors ($\langle\Delta\varphi\rangle$) are given for MAD phase sets determined from locally scaled, unmerged, diffraction amplitudes with ≥ 4 phase restraints per reflection (MAD 4, 8058 unique reflections), three phasing restraints per reflection (MAD 3, 1438 unique reflections), two phasing restraints per reflection (MAD 2, 4157 unique reflections). All experimental phase errors are defined relative to the 'true' phases calculated from the 1.6 Å resolution refined model of SiRHP (Crane & Getzoff, 1997). Values in parentheses are the errors in the experimental phases calculated with the Fe-atom positions from the final refined SiRHP model rather than the Fe-atom positions derived from the MAD data. For the MAD 4 reflection set, the probability treatment of *MADABCD* [$P(^{\circ}\varphi_T)$] results in only slightly more accurate phases than simply adding $^{\circ}\varphi_A$, determined from the anomalous scattering model, to $^{\circ}\varphi_T - ^{\circ}\varphi_A$ estimated from *MADLSQ* ($\Delta\varphi + ^{\circ}\varphi_A$). *MADLSQ*-derived phases with ≥ 4 restraints from the substandard data, collected either without the detector dead-time correction or on a decaying crystal, were calculated separately (MAD 4w, 851 reflections). When MAD intensities were reduced to an asymmetric unit prior to phase extraction and local scaling was not performed ($MAD_{nolocal}$), the completeness of unique reflections that can be phased by *MADLSQ* increases compared to MAD 4; however, the determined phases are not as accurate. If a phasing model analogous to isomorphous replacement is used instead of the *MADLSQ* least-squares procedure (MAD_{iso}), the overall completeness of unique reflections (Comp.) again increases compared with MAD 4, but again the phase accuracy also degrades. This is partly due to reflections not being required to have four or greater restraints and the lack of local scaling. When locally treated MAD phase sets are combined with one another (MAD_{comb}), inclusion of MAD 2 data increases completeness, but degrades phase quality [(4,4w,3,2) compared with (4,4w,3)]. The errors of MAD_{comb} phases are similar to errors of the multiple isomorphous replacement with anomalous scattering (MIRAS) phases dominated by the EMTS derivative (Crane *et al.*, 1995). Centroid phases determined from combination of MAD_{comb} (4,4w,3,2) and MIR phase distributions (MAD/MIRAS) gave the lowest phase errors and highest overall completeness. MAD/MIRAS amplitudes were taken from $\langle|F^{\pm}|\rangle$ of a Cu$K\alpha$ native data set collected on a rotating anode. $R_c = (\langle\rho_e\rho_r\rangle - \langle\rho_e\rangle\langle\rho_r\rangle)/\{[\langle\rho_e^2\rangle - \langle\rho_e\rangle^2]^{1/2}[\langle\rho_r^2\rangle - \langle\rho_r\rangle^2]^{1/2}\}$ is the correlation coefficient between the figure-of-merit (FOM) weighted experimental electron density (ρ_e), and the final $2F_o - F_c$ electron density phased with the refined structure (ρ_r). R_c reflects not only phase error, but also completeness of unique reflections phased and the FOM's used in weighting the structure factors.

Resolution (Å)	$\Delta\varphi + ^{\circ}\varphi_A$ $\langle\Delta\varphi\rangle$	MAD 4 $P(^{\circ}\varphi_T)$ $\langle\Delta\varphi\rangle$	Comp.	MAD 4w $\langle\Delta\varphi\rangle$	MAD 3 $\langle\Delta\varphi\rangle$	MAD 2 $\langle\Delta\varphi\rangle$	$MAD_{nolocal}$ $\langle\Delta\varphi\rangle$	Comp.	MAD_{iso} $\langle\Delta\varphi\rangle$	Comp.
∞–6.0	45.6 (45.4)	45.5 (45.2)	74.2	65.0 (57.7)	61.1 (65.8)	78.1 (77.4)	45.7 (47.2)	74.2	51.6 (51.2)	87.0
6.0–4.8	48.2 (44.8)	47.3 (43.7)	85.4	64.5 (57.5)	71.9 (71.0)	79.3 (76.8)	48.6 (51.7)	85.6	53.9 (52.2)	98.0
4.8–3.5	67.4 (60.0)	68.0 (60.5)	66.8	79.0 (71.3)	79.7 (79.5)	83.3 (85.3)	68.3 (64.1)	67.6	72.3 (67.2)	100.0
3.5–3.0	69.6 (60.0)	69.4 (59.5)	48.6	79.5 (73.8)	82.6 (77.9)	84.5 (83.0)	72.4 (66.8)	49.1	77.6 (70.5)	90.0
3.0–2.7	73.4 (65.2)	73.7 (66.1)	34.3	77.6 (73.8)	82.8 (77.2)	84.9 (81.7)	74.2 (69.7)	38.7	78.8 (72.6)	80.3
2.7–2.5	74.0 (64.5)	76.2 (66.3)	25.9	87.2 (82.1)	82.5 (81.3)	86.0 (85.3)	78.5 (72.1)	32.9	78.1 (74.0)	72.0
R_c	0.33 (0.44)	0.34 (0.41)					0.30 (0.33)		0.32 (0.37)	

Resolution (Å)	MAD_{comb} (4,4w,3,2) $\langle\Delta\varphi\rangle$	Comp.	MAD_{comb} (4w,4,3) $\langle\Delta\varphi\rangle$	Comp.	MIRAS $\langle\Delta\varphi\rangle$	Comp.	MAD/MIRAS $\langle\Delta\varphi\rangle$	Comp.
∞–6.0	48.4 (48.6)	82.2	46.3 (47.0)	76.9	46.3	100.0	42.9 (42.7)	100.0
6.0–4.8	50.2 (46.5)	95.2	46.9 (45.4)	89.8	52.2	100.0	45.4 (43.1)	100.0
4.8–3.5	71.7 (63.4)	85.5	67.4 (62.4)	72.7	66.1	100.0	64.4 (60.6)	100.0
3.5–3.0	74.8 (67.0)	71.2	70.7 (61.6)	55.0	70.7	100.0	68.9 (65.5)	100.0
3.0–2.7	78.6 (73.2)	60.1	73.6 (68.1)	39.8	80.4	96.9	77.4 (75.1)	100.0
2.7–2.5	80.7 (76.0)	53.4	75.6 (70.0)	32.1	86.4	91.4	84.2 (82.2)	97.3
R_c	0.34 (0.40)		0.36 (0.41)		0.35		0.43 (0.46)	

assess the source and magnitude of errors in intensity measurements. For the SiRHP MAD experiment, a few aberrant reflections were able to greatly skew the evaluation and treatment of our data.

To limit systematic error and extract anomalous signals from the SiRHP MAD experiment it was important to allow only observations collected closely together in time and reciprocal space to phase a given reflection (see Fig. 4). An experimental electron-density map with a higher map correlation coefficient resulted from the unmerged and locally scaled diffraction data ($R_c = 0.34$) than data that were reduced to an asymmetric unit before *MADLSQ* parameters were determined ($R_c = 0.30$, Table 5). It follows that significantly different intensity measurements among symmetry-related reflections were more detrimental to phase determination when the data were reduced to an asymmetric unit than when the data were not merged. These measured intensity differences were likely caused by pathlength- and orientation-dependent absorption of the relatively soft Fe-edge X-rays and time-dependent diffraction falloff from crystal decay. (Although the prevention of crystal decomposition by flash cooling in an N_2 cold stream is now an available option at beamline I-5AD, some protein crystals may not respond well to this treatment and thus crystal decay is likely to remain a problem.) Local scaling and local phase extraction are also beneficial for any experiment with low data redundancy where relative scale factors for swaths of reciprocal space and average intensities must be determined from a limited set of equivalent reflections. In contrast, for MAD experiments that use more penetrating radiation and have higher data multiplicity, reducing the data to an asymmetric unit before phase extraction may prove more successful than a local treatment. For example, in a MAD experiment where less absorption-sensitive uranium L_{III} edge X-rays were used to collect five to sevenfold redundant data on the OppA protein,

merging the diffraction amplitudes to an asymmetric unit produced the best phase estimates (Glover *et al.*, 1995). Thus, the most effective strategies for merging data during scaling and phase determination can depend upon the specifics of the MAD experiment.

The MAD experiment on SiRHP demonstrates that accurate estimation of local wavelength-independent parameters with the complete scattering equation requires enough well measured, independent observations to prevent indeterminacy. This problem is exemplified by the generation of large, unreasonable $|^{\circ}F_A|$ values when the least-squares equations are not well restrained. However, given a reasonably accurate global anomalous scattering model defined from well restrained, local MAD parameters, values for $|^{\circ}F_A|$ and $|^{\circ}F_T|$ can be estimated for reflections where the number of observations is insufficient to determine the linear system of equations used in *MADLSQ*. Unfortunately, the phase errors for these reflections are considerably worse than those for reflections with $\geq$4 observations (Table 5). The greater errors for reflections with $\leq$4 observations reflect not only the lack of overdetermination, but also increased sensitivity to positional error in the anomalous scattering model and the additional problem of scaling the $|^{\circ}F_A|_{\rm calc}$ values to the observed amplitudes. Terwilliger (Terwilliger, 1994*a*) has proposed a Bayesian approach to overcome the generation of large unreasonable estimates for $|^{\circ}F_A|$. For SiRHP, reflections with only two observations contain the largest phase errors (Table 5). Although combining this information with the other MAD data does degrade the overall phase quality, a greater number of reflections now supply some phase information for complementing the MIR distributions, resulting in marginally better overall MAD/MIR phases. Fig. 9 depicts how the number and type of restraints affect the phase probability distribution for an individual reflection. A centroid measure of $^{\circ}\varphi_T$ determined with *MADABCD* did not decrease phase error relative to simply adding $^{\circ}\varphi_A$ to the *MADLSQ*-derived ($^{\circ}\varphi_T - ^{\circ}\varphi_A$) value. The inability of the *MADABCD* treatment to improve phase estimates suggests that correlations between *MADLSQ* derived parameters biases the lack-of-closure based probability distributions towards the *MADLSQ*-derived ($^{\circ}\varphi_T - ^{\circ}\varphi_A$) value.

As our SiRHP results demonstrate, the success of MAD experiments that attempt to exploit the small anomalous signals of native metals in large proteins will depend on identifying and correctly modeling intrinsic errors. Defining and refining an accurate global anomalous scattering model is also key to accurate phase determination. The *MADLSQ* strategy can generate inaccurate parameter estimates if only a few observations contribute to estimating the local phasing parameters for a given reflection. These potentially inaccurate parameters together then contribute to defining the global anomalous scattering model. With a relatively small signal-to-noise ratio, a more global approach, analogous to traditional MIR phasing protocols, may be preferable. In this case, all observations simultaneously determine global parameters for the anomalous scattering model before phases are derived. For SiRHP MAD data, such an MIR-related strategy was less successful at determining phases than the *MADLSQ* procedure. However, as implemented, this approach suffered from overweighting of the 'native' data set and globally scaling together data sets from different wavelengths. As well, correlations that exist among calculated anomalous differences due to a mutual dependence on $^{\circ}\varphi_T$ and the anomalous scatterer parameters can bias phase and positional refinement and lead to the underestimation of phase errors. Nevertheless, in the context of a suitable probability model, approaches analogous to MIR have proven quite successful for phasing structures from MAD data (Ramakrishnan, Finch, Graziano, Lee & Sweet, 1993; Terwilliger, 1994*b*; Glover *et al.*, 1995). In the companion paper (Crane & Getzoff, 1997), refinement of the SiRHP global anomalous scattering model directly against observed Bijvoet and dispersive differences is shown to be highly effective at phase determination and is also used to confirm an asymmetry of the Fe_4S_4 cluster found in the 1.6 Å resolution SiRHP refined structure.

Ultimately, the ability to phase a macromolecular structure from MAD resides in the quality of the diffraction data collected. In addition to the size and order of the crystal itself, data quality reflects source intensity, data multiplicity, and crystal stability in the X-ray beam. Improvements in synchrotron sources, instrumentation and data analysis, coupled with the growing base of methodological information obtained from this and other MAD experiments, promises to make MAD an accessible and effective means of macromolecular phase determination even on less than ideal systems.

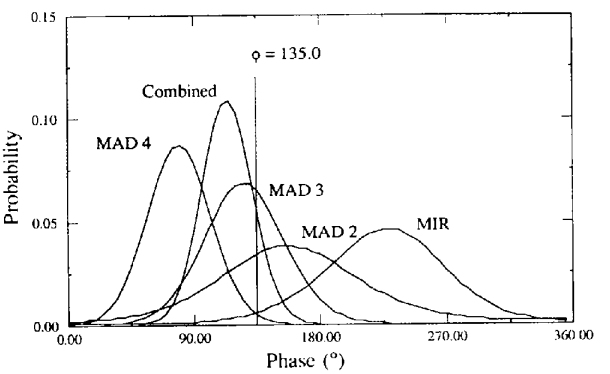

Fig. 9. The accuracy and width of phase probability distributions are affected by the number and type of observational restraints. Probability distributions for reflection *hkl* = 4,7,14 taken from local scaling shifts that provide six (MAD $\geq$4), three (MAD 3) and two (MAD 2) phasing restraints are shown with the MIR-derived distribution (MIR), the total combined distribution (Combined), and position of the true phase calculated from the refined model (135.0°).

We thank J. A. Tainer, R. P. Phizackerley, W. A. Hendrickson, C. Nielsen, D. E. McRee, J. W. Pflugrath, E. A. Merritt, W. I. Weis and T. C. Terwilliger for helpful discussions and advice; M. E. Pique, T. J. Macke and A. S. Arvai for assistance with computation; and the Stanford Synchrotron Radiation Laboratory for the use of data-collection facilities. We note that SSRL beamline I-5AD has been upgraded to optimize collection of strong redundant MAD data. The beam is now focused in two dimensions by a bent cylindrical rhodium-coated mirror which provides ~20 times more flux than before. The multiwire detector has been replaced by Fuji image plates mounted on a rotation camera carousel and a cryocooling system has also been added to ameliorate difficulties encountered from crystal radiation sensitivity. This work was supported by NIH grant GM37684 to EDG and an NSERC fellowship to BRC.

References

Brünger, A. T., Kuriyan, J. & Karplus, M. (1987). *Science*, **235**, 458–460.

Collaborative Computational Project, Number 4 (1994). *Acta Cryst.* D**50**, 760–763.

Crane, B. R. & Getzoff, E. D. (1997). *Acta Cryst.* D**53**, 23–40.

Crane, B. R., Siegel, L. M. & Getzoff, E. D. (1995). *Science*, **270**, 59–67.

Eichhorn, K. D. (1985). *DISCO*. Stanford Synchrotron Radiation Laboratory, USA.

Fox, G. C. & Holmes, K. C. (1966). *Acta Cryst.* **20**, 886–891.

Furey, W. & Swaminathan, S. (1990). Am. Crystallogr. Assoc. Meet. New York. p. 73.

Glover, I. D., Denny, R. C., Nguti, N. D., McSweeney, S. M., Kinder, S. H., Thompson, A. W., Dodson, E. J., Wilkinson, A. J. & Tame, J. R. H. (1995). *Acta Cryst.* D**51**, 39–47.

Güss, J. M., Merritt, E. A., Phizackerley, R. P., Hedman, B., Murata, M., Hodgson, K. O. & Freeman, H. C. (1988). *Science*, **241**, 806–811.

Hamlin, R. (1985). *Methods Enzymol.* **114**, 416–452.

Hendrickson, W. A. (1991). *Science*, **254**, 51–58.

Hendrickson, W. A. & Lattman, E. A. (1970). *Acta Cryst.* B**26**, 136–143.

Hendrickson, W. A., Pähler, A., Satow, Y., Merritt, E. A. & Phizackerley, R. P. (1989). *Proc. Natl Acad. Sci. USA*, **86**, 2190–2194.

Hendrickson, W. A., Smith, J. L., Phizackerley, R. P. & Merritt, E. A. (1988). *Proteins Struct. Funct. Genet.* **4**, 77–88.

Howard, A. J., Nielsen, C. & Xuong, N. H. (1985). *Methods Enzymol.* **114**, 452–472.

James, R. W. (1965). In *The Optical Principles of the Diffraction of X-rays. The Crystalline State*, Vol. 2. New York: Cornell University Press.

Kabsch, W. J. (1988). *J. Appl. Cryst.* **21**, 916–924.

Kraut, J. (1968). *J. Mol Biol.* **35**, 511–512.

McRee, D. E. (1992). *J. Mol. Graphics*, **10**, 44–46.

McRee, D. E., Richardson, D. C., Richardson, J. S. & Siegel, L. M. (1986). *J. Biol. Chem.* **261**, 10277–10281.

Messerschmidt, A. & Pflugrath, J. W. (1987). *J. Appl. Cryst.* **20**, 306–315.

Monahan, J. E., Schiffer, M. & Schiffer, J. P. (1967). *Acta Cryst.* **22**, 322–322.

Murthy, H. M. K., Hendrickson, W. A., Orme-Johnson, W. H., Merritt, E. A. & Phizackerley, R. P. (1988). *J. Biol. Chem.* **263**, 18430–18436.

Pähler, A., Smith, J. L. & Hendrickson, W. A. (1990). *Acta Cryst.* **A46**, 537–540.

Peck, Jr, H. D. & Lissolo, T. (1988). *Forty-Second Symposium of The Society For General Microbiology – The Nitrogen and Sulphur Cycles*, edited by J. A. Cole & S. J. Ferguson, Vol. 42, pp. 99–132. Cambridge University Press.

Phizackerley, R. P., Cork, C. W. & Merritt, E. A. (1986). *Nucl. Instrum. Methods*, **246**, 579–595.

Powell, M. J. D. (1977). *Math. Program.* **12**, 241–254.

Ramakrishnan, V., Finch, J. T., Graziano, V., Lee, P. L. & Sweet, R. M. (1993). *Nature (London)*, **362**, 219–223.

Siegel, L. M. & Davis, P. S. (1974). *J. Biol. Chem.* **249**, 1587–1598.

Smith, J. L., Zaluzec, E. J., Wery, J., Niu, L., Switzer, R. L., Zalkin, H. & Satow, Y. (1994). *Science*, **264**, 1427–1433.

Terwilliger, T. C. (1994*a*). *Acta Cryst.* D**50**, 11–16.

Terwilliger, T. C. (1994*b*). *Acta Cryst.* D**50**, 17–23.

Upson, C., Faulhabe, T., Kamins, D., Laidlaw, D., Schlegel, D., Vroom, J., Gurwitz, R. & Vandam, A. (1989). *IEEE Comp. G*, **9**, 30–42.

Weis, W. I., Kahn, R., Fourme, R., Drickamer, K. & Hendrickson, W. A. (1991). *Science*, **254**, 1608–1615.

Xuong, N. H., Nielsen, C., Hamlin, R. & Anderson, D. (1985). *J. Appl. Cryst.* **18**, 342–350.

Yang, W., Hendrickson, W. A., Crouch, R. J. & Satow, Y. (1990). *Science*, **249**, 1398–1405.